Vol. 51 (2020) *Acta Physica Polonica B* No 6

SOFT QCD AT ATLAS AND CMS*

Yuri Kulchitsky

on behalf of the ATLAS and CMS collaborations

JINR, Dubna, Russia
and
Institute of Physics, National Academy of Sciences, Minsk, Belarus
Yuri.Koultchitski@cern.ch

(Received May 18, 2020)

A short overview of the recent results of soft QCD measurements in proton–proton collisions from the ATLAS and CMS collaborations at the Large Hadron Collider is presented. Measurements of double parton scattering and the underlying event in inclusive production, and differential cross sections for single diffractive dissociation at centre-of-mass energies $\sqrt{s} = 8$ and 13 TeV are discussed.

DOI:10.5506/APhysPolB.51.1411

1. Introduction

Hard Quantum Chromodynamics (QCD) events constitute only a tiny fraction of the total proton–proton (*pp*) cross section, which is dominated by soft events (peripheral processes). The hard scattering processes have a momentum transfer sufficiently large that the strong coupling constant is small and the cross section may be calculated perturbatively in QCD, which is not possible for soft QCD events. Soft QCD measurements are crucial for the tuning of Monte Carlo (MC) event generators and essential to understand and correctly simulate other more complex phenomena. Most of the soft QCD analyses are track-based measurements, which makes them ideal to study tracking performance in the early stages of a new data-taking period. In the paper, a short overview of the recent results of soft QCD measurements in *pp* collisions from the ATLAS [1] and CMS [2] collaborations at the Large Hadron Collider (LHC) [3] is presented.

* Presented at XXVI Cracow Epiphany Conference on LHC Physics: Standard Model and Beyond, Kraków, Poland, January 7–10, 2020.

2. Double-parton scattering in pp collisions

The inclusive production of four isolated charged leptons in pp collisions is analysed for the presence of hard double-parton scattering (DPS), using 20.2 fb^{-1} of data recorded in the ATLAS detector at the LHC at a centre-of-mass energy of $\sqrt{s} = 8$ TeV [4]. In the four-lepton ($4l$) invariant-mass range of $80 < m_{4l} < 1000$ GeV, an artificial neural network (ANN) is used to enhance the separation between single-parton scattering (SPS) and DPS based on the kinematic properties of the $4l$ in the final state. The output of the ANN, ξ^{DPS}, is a number distributed between 0 and 1, which represents the likelihood for an event to belong to the DPS class. The trained ANN is applied to data events, and the resulting distribution of ξ^{DPS} is shown in figure 1 (left), together with the corresponding DPS, SPS and background MC distributions. The DPS MC events form a peak around $\xi^{\mathrm{DPS}} = 1$ and

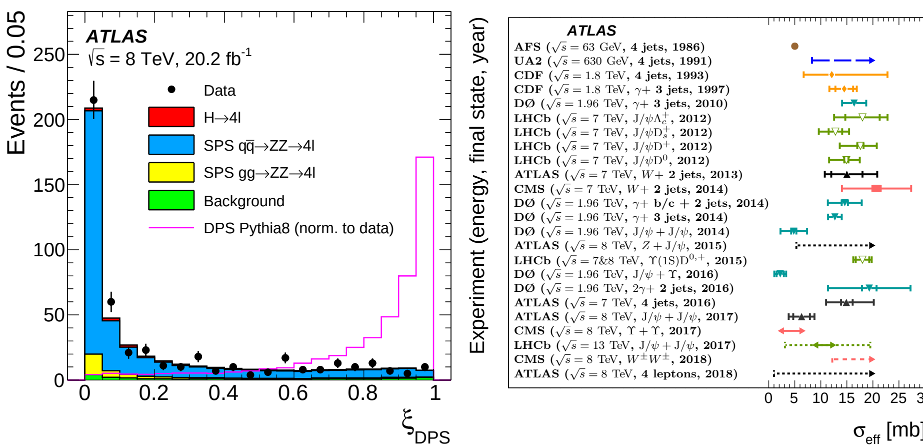

Fig. 1. (Colour on-line) Left: The distribution of the output variable of the ANN, ξ^{DPS}. Right: Summary of measurements and limits on the effective cross section sorted chronologically. The measurements that were made by different experiments are denoted by different symbols and colours. The inner error bars represent statistical uncertainties. The outer error bars correspond to the total uncertainty. Dashed arrows indicate lower limits. Lines with arrows on both ends represent ranges of the effective cross-section values. Taken from Ref. [4].

the SPS and background events form a peak at $\xi^{\mathrm{DPS}} = 0$, as expected. A similar peak at $\xi^{\mathrm{DPS}} = 0$ is observed in data events, with no indication of a substantial contribution of DPS at $\xi^{\mathrm{DPS}} = 1$. In order to quantify the level of the potential DPS contribution in the data, the variable f_{DPS} is introduced, defined as the ratio of the number of DPS events, $N_{\mathrm{DPS},4l}$, to the sum of the DPS and SPS, ($N_{\mathrm{SPS},4l}$): $f_{\mathrm{DPS}} = N_{\mathrm{DPS},4l}/(N_{\mathrm{SPS},4l} + N_{\mathrm{DPS},4l})$.

The upper limit (UL) on $f_{\rm DPS}$ is determined using the distributions of the $\xi^{\rm DPS}$ variable in data, SPS, DPS, and background MC samples. The value of the UL on $f_{\rm DPS}$ found at 95% confidence level (CL) is 0.042. The UL on $f_{\rm DPS}$ can be transformed into a lower limit (LL) on $\sigma_{\rm eff}$ by using the equation: $\sigma^{AB}_{\rm DPS} = 0.5k\,(\sigma^{A}_{\rm SPS}\sigma^{B}_{\rm SPS})/\sigma_{\rm eff}$. In this equation, $\sigma^{A(B)}_{\rm SPS}$ denotes the production cross section of state A (B) in SPS in the process $pp \to A + B + X$. The k is the symmetry factor which depends on whether the two scatterings lead to the same final state ($A = B$, $k = 1$) or different final states ($A \neq B$, $k = 2$). The $\sigma_{\rm eff}$ represents the effective transverse overlap area containing the interacting partons. Therefore, the $\sigma_{\rm eff}$ may be defined as: $1/\sigma_{\rm eff} = f_{\rm DPS}\,\sigma^{4l}/(0.5k\,\sigma^{A}_{\rm SPS}\sigma^{B}_{\rm SPS})$, and hence an approach similar to that used for the extraction of the upper limit on $f_{\rm DPS}$ can be applied to set the LL on $\sigma_{\rm eff}$, which at 95% CL is 1.0 mb, and consistent with previously measured values of the effective cross section, as shown in figure 1 (right).

A study of WW production from DPS processes, using the same-charge dimuon ($\mu^{\pm}\mu^{\pm}$) and electron–muon ($e^{\pm}\mu^{\pm}$) events is carried out using pp collision data at $\sqrt{s} = 13$ TeV [5]. The analysed data set corresponds to an integrated luminosity of 77 fb^{-1}, collected with the CMS detector. Multivariate classifiers are used to discriminate between the signal and the dominant background processes. A maximum likelihood fit is performed separately for different lepton charge configurations and their combination. The obtained values of the DPS $W^{\pm}W^{\pm}$ cross section are then extrapolated to the inclusive WW phase space and are shown in figure 2, with the expected value for $\sigma^{WW}_{\rm DPS}$ taken from PYTHIA 8 [6] and the factorization approach. The pos-

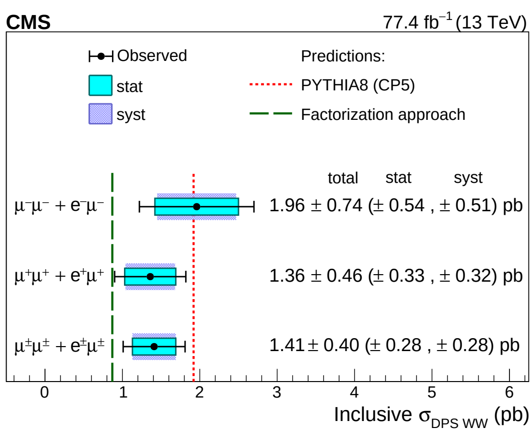

Fig. 2. (Colour on-line) Observed cross-section values for inclusive DPS WW production from the two lepton charge configurations and their combination. The predictions from PYTHIA 8 and the factorization approach are represented using dotted/red and dashed/green lines, respectively. Taken from Ref. [5].

itive charge configuration results in a measured inclusive cross section of $1.36 \pm 0.33\,(\mathrm{stat.}) \pm 0.32\,(\mathrm{syst.})$ pb and for the negative charge configuration, the value is $1.96 \pm 0.54\,(\mathrm{stat.}) \pm 0.51\,(\mathrm{syst.})$ pb. A measurement of the DPS WW cross section is achieved for the first time, and a cross section of $1.41 \pm 0.28\,(\mathrm{stat.}) \pm 0.28\,(\mathrm{syst.})$ pb is extracted with an observed significance of 3.9 standard deviations.

3. Underlying event in inclusive production in *pp* collisions

The measurements of charged-particle distributions sensitive to the properties of the underlying event (UE) in events containing a Z boson decaying into a muon pair are presented in Ref. [7]. The data were obtained using the ATLAS detector at the LHC in pp collisions at 13 TeV with an integrated luminosity of 3.2 fb^{-1}. Distributions of the charged-particle multiplicity and of the charged-particle transverse momentum are measured in regions of the azimuthal angle defined relative to the Z-boson direction. The MC modelling of individual measurements in 96 phase-space regions is further investigated by comparing the measured arithmetic means of N_{ch}, $\sum p_{\mathrm{T}}$, and mean p_{T} as functions of p_{T}^{Z} with (left) $T_{\perp} < 0.75$ and (right) $T_{\perp} > 0.75$ for the trans-min region. Transverse thrust characterizes the topology of the tracks in the event and is given by $T_{\perp} = \sum_i |\vec{p}_{\mathrm{T},i} \cdot \hat{n}| / \sum_i |\vec{p}_{\mathrm{T},i}|$, where the thrust axis $\hat{n}$ is the unit vector which maximizes $T_{\perp}$[1]. Figure 3 shows comparisons of the N_{ch} distributions with the predictions of POWHEG [8] with PYTHIA 8, Sherpa [9], and Herwig++ [10] for the trans-min and towards regions inclusively in $T_{\perp}$. The predictions fail to describe the data in either of the regimes. For $p_{\mathrm{T}}^{Z} > 20$ GeV, Herwig++ predicts a slower rise in UE activity with rising p_{T}^{Z} than in the measured distributions. On the other hand, POWHEG+PYTHIA 8 and Sherpa qualitatively describe the "turn-on" effect of the UE activity, *i.e.* a steeper slope at low p_{T}^{Z} which vanishes at higher values of p_{T}^{Z}. For POWHEG+PYTHIA 8, the rise of the UE activity is underestimated, and hence the discrepancy with data grows with p_{T}^{Z} and stabilizes around $p_{\mathrm{T}}^{Z} = 100$ GeV. Only in the toward region of the mean p_{T} is Sherpa in good agreement with the data. Figure 4 presents a comparison of the measured (left) N_{ch} and (right) $\sum p_{\mathrm{T}}$ for different $\sqrt{s}$. The results for $\sqrt{s} = 7$ TeV are taken from the previous ATLAS measurement of the UE activity in Z-boson events [11]. The event selection criteria are similar to the analysis presented in Ref. [7], but Ref. [11] also includes the $Z \to e^+e^-$ channel. The results are also compared with CDF measurements at 1.96 TeV [12], which used the Drell–Yan lepton pairs in a smaller invariant mass window ($70 < m_{\mu\mu} < 110$ GeV). The relative uncertainties of the two ATLAS

[1] Transverse thrust has a maximum of 1 for a pencil-like dijet topology and a minimum of $2/\pi$ for a circularly symmetric distribution of particles in the transverse plane.

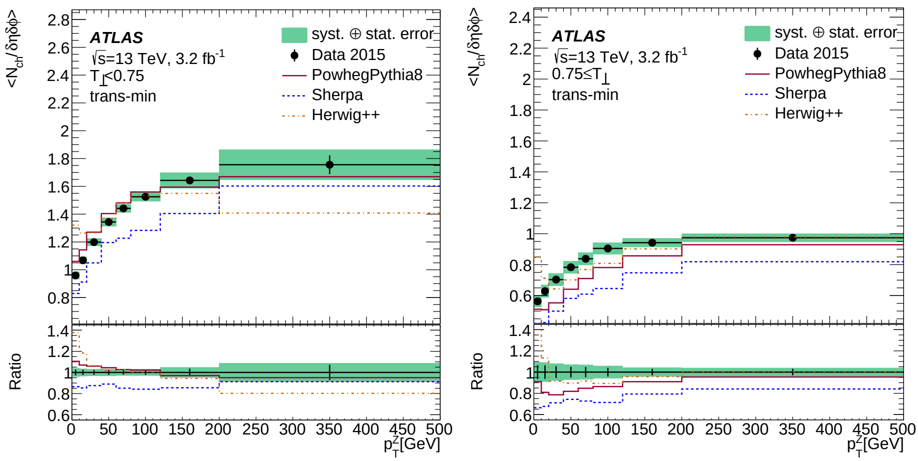

Fig. 3. Comparison of measured arithmetic means of N_{ch} as functions of p_{T}^{Z} for (left) $T_{\perp} < 0.75$ and (right) $T_{\perp} > 0.75$ for the trans-min region. Predictions of POWHEG with PYTHIA 8, Sherpa and Herwig++ are compared with the data. The ratios shown are predictions over data. Taken from Ref. [7].

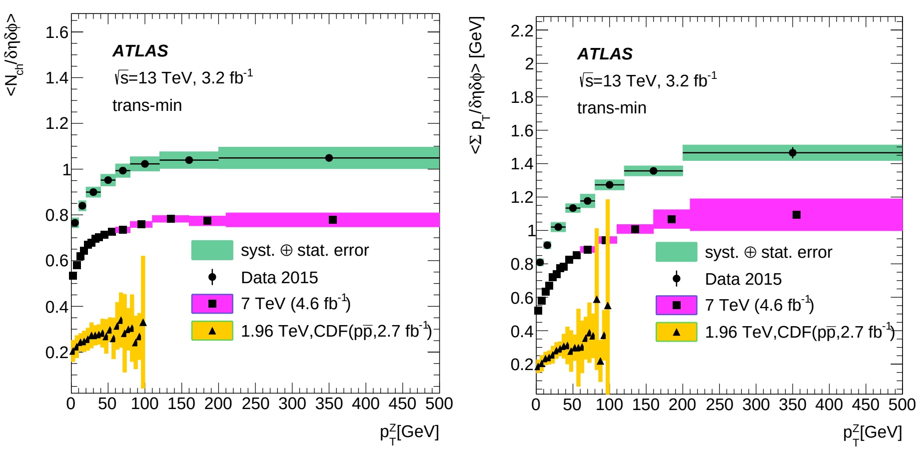

Fig. 4. The distributions of (left) N_{ch} and (right) $\sum p_{\mathrm{T}}$ measured at 13 TeV compared with the ATLAS results at 7 TeV [11] and the CDF measurements at 1.96 TeV [12]. Taken from Ref. [7].

measurements are of similar sizes, while the CDF measurements have large statistical fluctuations for $p_{\mathrm{T}}^{Z/\mu\mu} > 30$ GeV. All three measurements reveal the turn-on effect of the UE activity in the fiducial region (FR). With higher $\sqrt{s}$, more energy is available for the processes forming the UE *e.g.* Multi-Parton Interactions (MPI). Hence, the rise of the UE activity as a function of $\sqrt{s}$ is expected.

The measurement of the UE activity in pp collisions at $\sqrt{s} = 13$ TeV with an integrated luminosity of 2.1 fb^{-1}, performed using inclusive Z-boson production events collected with the CMS experiment at the LHC are presented in Ref. [14]. The UE activity is quantified in terms of the charged particle multiplicity of the scalar sum of the charged particles transverse momenta in different topological regions defined with respect to the Z-boson direction. The distributions are unfolded to the stable particle level and compared with predictions from various MC event generators. To understand the evolution of the UE activity with $\sqrt{s}$, the present measurement is compared with results obtained at 1.96 TeV (CDF) and at 7 TeV (CMS). As the away region is dominated by the jet balancing the Z boson, the particle activity in this region is not considered for this specific study. Figure 5 shows the UE activity as a function of $p_{\mathrm{T}}^{\mu\mu}$ at 1.96, 7, and 13 TeV. The predictions of POWHEG+PYTHIA 8 and POWHEG+Herwig++ are also shown. The ratios of the simulations to the measurements are plotted in the bottom panel of each plot. The POWHEG+PYTHIA 8 predictions reproduce the measurements within 10% at $\sqrt{s} = 1.96$ and 7 TeV, and within 5% at 13 TeV. The combination of POWHEG+Herwig++ describes the measurements within 10–15, 10–20, and 20–40% at $\sqrt{s}$ of 1.96, 7, and 13 TeV, respectively. To further quantify the energy dependence of the UE activity, events with a $p_{\mathrm{T}}^{\mu\mu}$ smaller than 5 GeV are studied. Setting an UL on $p_{\mathrm{T}}^{\mu\mu}$ reduces the ISR and FSR contributions, and the remaining UE activity stems mainly from MPI. With the requirement of $p_{\mathrm{T}}^{\mu\mu} < 5$ GeV, the UE activity is similar in the towards and transverse regions. Therefore, the UE activity is combined in these two regions. Figure 6 shows the UE activity, with the $p_{\mathrm{T}}^{\mu\mu} < 5$ GeV requirement, as a function of $\sqrt{s}$ for data compared to model predictions. There is a significant increase, by a factor of 2–2.5, as the collision energy rises from 1.96 to 13 TeV, which is qualitatively reproduced by POWHEG. The energy evolution is better described by POWHEG+PYTHIA 8, whereas hadronization with Herwig++ overestimates the UE activity at all collision energies. The comparison of the distributions with and without MPI indicates that the ISR and FSR contributions, which increase slowly with $\sqrt{s}$, are small. The CUETP8M1 [15] and EE5C [16] tunes employed here are mostly obtained from fits to minimum-bias measurements and UE measurements with leading jets or leading tracks. The fact that these tunes reproduce globally well the present data supports the hypothesis that the UE activity is independent of the hard process. The present study also confirms that the collision energy dependence of the UE activity is similar for different hard processes. Unlike UE studies with a leading track/jet, the present measurements provide new handles to better understand the evolution of ISR, FSR, and MPI contributions separately, as functions of the event energy scale and the collision energy.

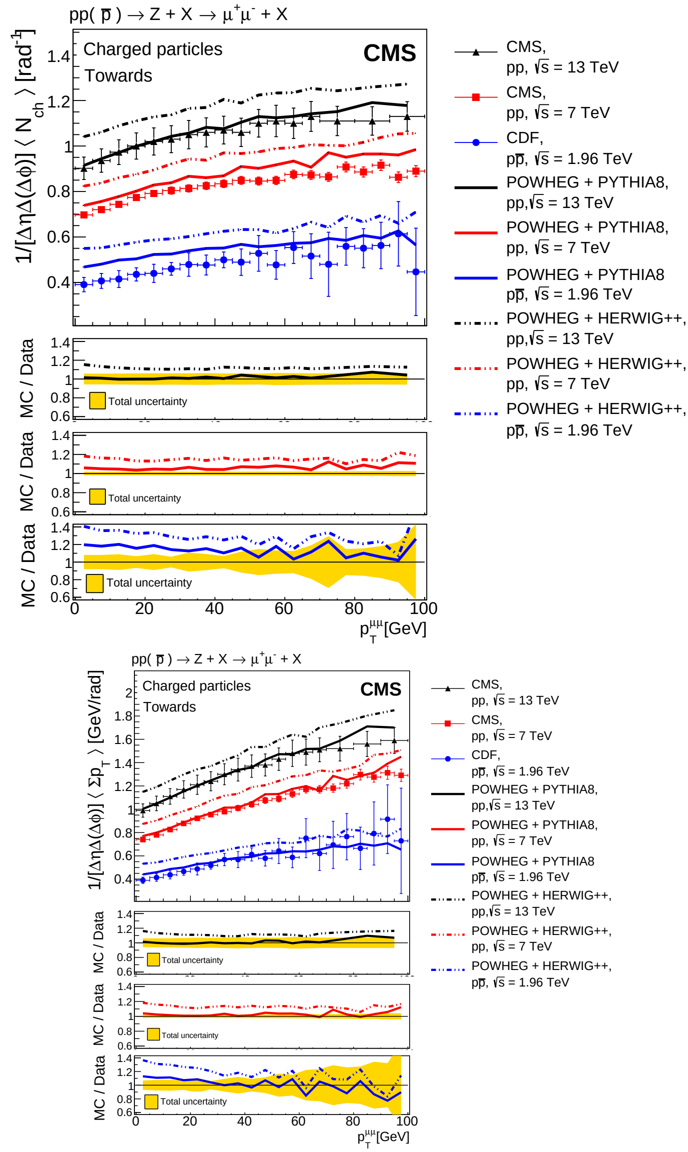

Fig. 5. Comparison of (top) the particle density and (bottom) p_{T} measured in Z events at 13 TeV with that at 7 TeV (CMS) [13] and 1.96 TeV (CDF) [12] in the *towards* region as a function of $p_{\mathrm{T}}^{\mu\mu}$. The data are also compared with the model predictions of POWHEG+PYTHIA 8 (solid line) and POWHEG+Herwig++ (dash-dotted line). The bottom panels of each plot show the ratios of the model predictions to the measurements. The bands in the bottom panels represent the statistical and systematic uncertainties added in quadrature. Taken from Ref. [14].

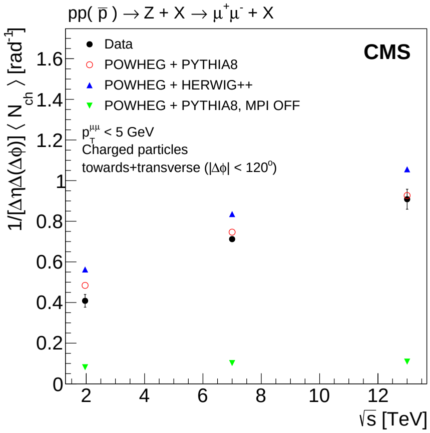

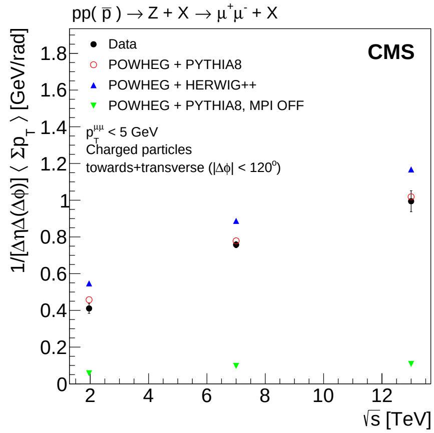

Fig. 6. (Left) Average particle density and (right) average $\sum p_{\mathrm{T}}$ density for Z events with $p_{\mathrm{T}}^{\mu\mu} < 5$ GeV as a function of the $\sqrt{s}$, measured by CMS and CDF [12] in the combined towards + transverse regions, compared to predictions from POWHEG+PYTHIA 8, POWHEG+Herwig++, and POWHEG+PYTHIA 8 without MPI. Taken from Ref. [14].

Measurements of normalized differential cross sections as functions of the multiplicity and kinematic variables of charged-particle tracks from the UE in top-quark and antiquark pair production are presented in Ref. [17]. The measurements are performed in pp collisions at $\sqrt{s} = 13$ TeV, and are based on data collected by the CMS experiment at the LHC corresponding to an integrated luminosity of 35.9 fb^{-1}. Events containing one electron, one muon, and two jets from the hadronization and fragmentation of b quarks are used. These measurements characterize, for the first time, properties of the UE in top-quark pair production and show no deviation from the universality hypothesis at energy scales typically above twice the top-quark mass. The average total energy as well as the hadronic and electromagnetic components of it are measured with the CMS detector in the pseudorapidity region of $-6.6 < \eta < -5.2$ in pp collisions at $\sqrt{s} = 13$ TeV and are presented in Ref. [18]. The results are shown as a function of the multiplicity of charged particle tracks in the region $|\eta| < 2$. This measurement is sensitive to correlations induced by the UE structure over very wide pseudorapidity regions. It is very interesting that some of the most recent event generator tunes have the largest tension with respect to the data.

4. Differential cross sections for single diffractive dissociation

A dedicated sample of the LHC pp collision data at $\sqrt{s} = 8$ TeV is used to study inclusive single diffractive (SD) dissociation, $pp \to X + p$ [19].

The intact final-state proton is reconstructed in the ATLAS ALFA forward spectrometer, while charged particles from the dissociated system X are measured in the central detector components. Cross sections are measured differentially as functions of the proton fractional energy loss ξ, the squared four-momentum transfer t, and $\Delta\eta$. A variable $\Delta\eta$ characterises the rapidity gap (RG) separating the proton and the system X in which no primary[2] charged particles are produced with $p_{\mathrm{T}} > 200$ MeV. The unfolded hadron-level SD cross sections are integrated over the FR $-4.0 < \log_{10}\xi < -1.6$ and $0.016 < |t| < 0.43$ GeV^2, and correspond to cases where either of the two protons dissociates. The SD differential cross section as a function of $\Delta\eta$ is presented in figure 7 (left). For RG sizes between about 1.5 and 3.5,

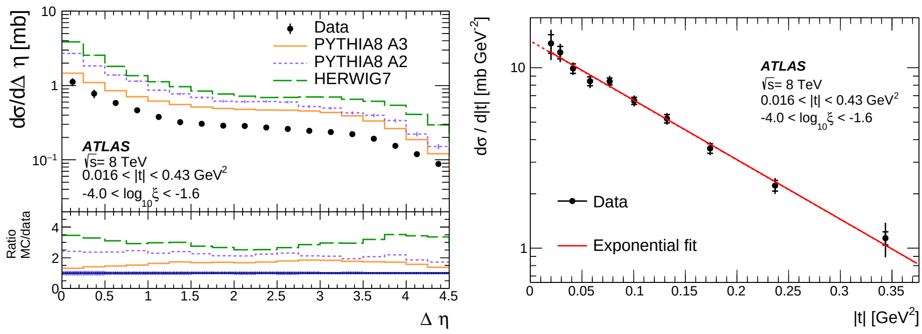

Fig. 7. Left: Hadron-level differential SD cross section as a function of $\Delta\eta$, comparing the measured data with PYTHIA 8 and Herwig 7 predictions. Right: The differential cross section as a function of $|t|$ with inner error bars representing statistical uncertainties and outer error bars displaying the statistical and systematic uncertainties added in quadrature. Taken from Ref. [19].

the differential cross section exhibits the plateau that is characteristic of RG distributions in soft diffractive processes. There are deviations from this behaviour at smaller and larger gap sizes due to the definition of the observable in terms of a restricted rapidity region corresponding to the inner detector (ID) acceptance, and to the FR restriction, respectively. The data are compared with the SD process simulations in the PYTHIA 8 A2 [20] and A3 [21] tunes, which exceed the measurement by factors of 2.3 and 1.5, respectively. Both models give a reasonable description of the shape of the $\Delta\eta$ distribution, with the PYTHIA 8 A2 tune being slightly better. The Herwig 7 prediction is also broadly in line with the shape of the $\Delta\eta$ distribution. The cross section is shown differentially in $|t|$ in figure 7 (right).

[2] A primary charged particle is defined as a charged particle with a mean proper lifetime $\tau > 300$ ps, which is either directly produced in pp interactions or from decays of directly produced particles with $\tau < 30$ ps.

To avoid bias in the fit due to the fast-falling nature of the distribution, the data points are plotted at the average values of $|t|$ in each bin. The data are consistent with an exponential t dependence, $\mathrm{d}\sigma/\mathrm{d}t \propto \mathrm{e}^{Bt}$ with slope parameter $B = 7.65 \pm 0.34\,(\mathrm{stat.}) \pm 0.22\,(\mathrm{syst.})$ GeV^{-2}. The measured parameter B corresponds to a value averaged over the ξ FR, with $\langle \log_{10} \xi \rangle = -2.88 \pm 0.14$, where the central value is taken from the PYTHIA 8 A3 and the uncertainty is defined by the difference from the A2.

In figure 8, the cross section is shown differentially in $\log_{10} \xi$, as obtained from the charged particles reconstructed in the ID. Fully compatible results are obtained when reconstructing ξ using ALFA, despite the fast-deteriorating resolution at small ξ values and completely different systematic effects. The data are compatible with being independent of this variable, characteristic of the expected behaviour of the cross section roughly as $\mathrm{d}\sigma/\mathrm{d}\xi \sim 1/\xi$. A more detailed interpretation of the ξ dependence is obtained through a fit to the data in the framework of Regge phenomenology. At asymptotically large fixed s, and with $s \gg M_X^2 \gg |t|$, the double-differential cross section in ξ and t is expected to follow the "triple Regge" form. The ID-track-based measurement is adopted and the standard triple Pomeron approach of Regge phenomenology is used to describe the data in terms of a Pomeron trajectory with intercept $\alpha(0) = 1.07 \pm 0.09$, in good agreement with previous values from ATLAS and elsewhere. The measured cross section integrated over the FR amounts to 1.59 ± 0.13 mb.

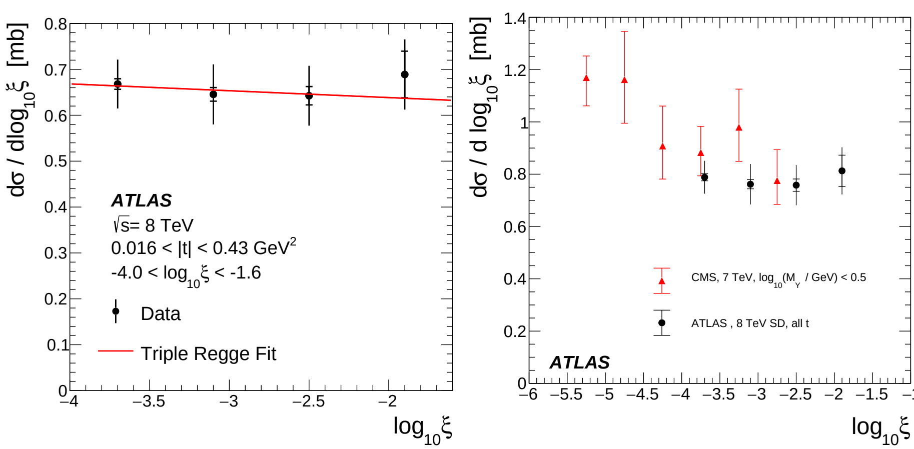

Fig. 8. The differential cross section as a function of $\log_{10} \xi$. Left: Data in the t FR, compared with the results of the triple Regge fit. Right: ATLAS data extrapolated to the full t range, compared with an RG-based CMS measurement [22] that contains a small DD admixture. Taken from Ref. [19].

A study of dijet production associated with a leading proton is presented in Ref. [23]. The analysis is based on a common data set collected simultaneously with the CMS and TOTEM detectors at the LHC with pp collisions at $\sqrt{s} = 8$ TeV during a dedicated run with $\beta^* = 90$ m, at low instantaneous luminosity. The data correspond to an integrated luminosity of 37.5 nb^{-1}. The analysis presents the measurement of the dijet production cross section, as a function of x, the proton fractional momentum loss, and as a function of t, the 4-momentum transfer squared at the proton vertex. The dijet cross section in the kinematic region defined by $x < 0.1$, $0.03 < |t| < 1$ GeV^2, with at least two jets with transverse momentum $p_{\mathrm{T}} > 40$ GeV, and pseudorapidity $|\eta| < 4.4$, is measured as $21.7 \pm 0.9\,(\mathrm{stat.})^{+3.0}_{-3.3}\,(\mathrm{syst.}) \pm 0.9\,(\mathrm{lumi.})$ nb. Both the processes $pp \to p + X$ and $pp \to X + p$ are measured, with X including a system of two jets. The results correspond to the average of their cross sections. The ratio of the SD to inclusive dijet yields, normalised per unit of x, is presented as a function of x, the longitudinal momentum fraction of the proton carried by the struck parton. The ratio in the kinematic region defined above, for x values in the range of $-2.9 \leq \log_{10} x \leq -1.6$, was measured as $R = (\sigma^{pX}_{jj}/\Delta\xi)/\sigma_{jj} = 0.025 \pm 0.001\,(\mathrm{stat.}) \pm 0.003\,(\mathrm{syst.})$. The results are compared to the predictions from models of diffractive and non-diffractive (ND) interactions. Figure 9 (left) shows the ratio $R(x)$, calculated in the kinematic region $p_{\mathrm{T}} > 40$ GeV, $|\eta| < 4.4$, $\xi < 0.1$ and $0.03 < |t| < 1$ GeV^2 and $-2.9 \leq \log_{10} x \leq -1.6$. The average of the results for events in which

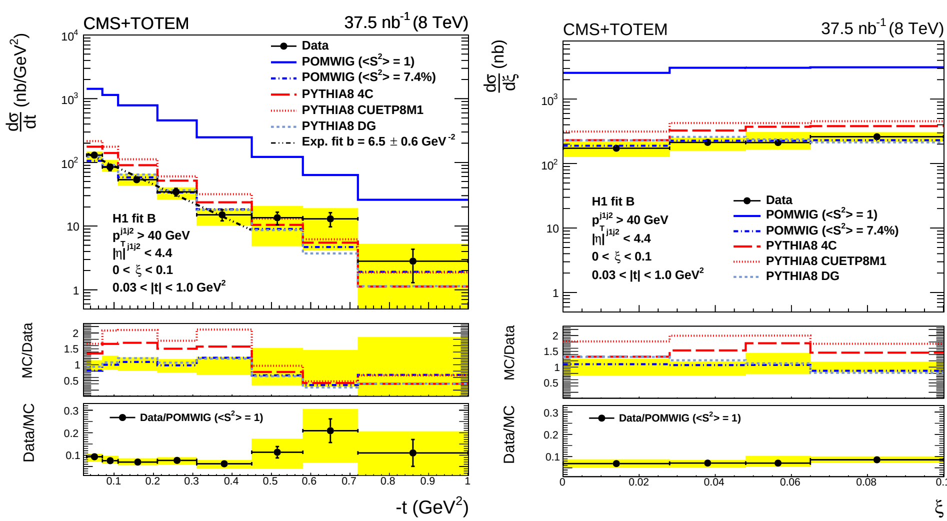

Fig. 9. (Colour on-line) Differential cross section as a function (left) of t and (right) ξ for SD dijet production, compared to the predictions from POMWIG, PYTHIA 8 4C, PYTHIA 8 CUETP8M1 and PYTHIA 8 DG. Taken from Ref. [23].

the proton is detected on either side of the interaction point is shown. The grey/yellow band represents the systematic uncertainties. The data are compared to the ratio of the SD and ND cross sections from different models. The SD contribution is simulated with POMWIG [24], PYTHIA 8 with 4C and CUETP8M1 tunes [25], and PYTHIA 8 Dynamic Gap (DG) [26]. The ND contribution is simulated with PYTHIA 6 [27] and Herwig 6 [28] when POMWIG was used as the diffractive contribution. When using PYTHIA 8, the diffractive and ND contributions are simulated with the same UE tune. When no correction for the RG survival probability is applied ($\langle S^2 \rangle = 1$), POMWIG shows cross sections higher by roughly an order of magnitude. Figure 10 (right) compares the results in figure 10 (left) with those from CDF [29]. The CDF results are shown for jets with $Q^2 \approx 100$ GeV^2 and $|\eta| < 2.5$, with $0.03 < \xi < 0.09$. In this case, Q^2 is defined, per event, as the mean transverse energy of the two leading jets squared. CDF measures the ratio for Q^2 values up to 104 GeV^2. A relatively small dependence on Q^2 is observed. The present data are lower than the CDF results.

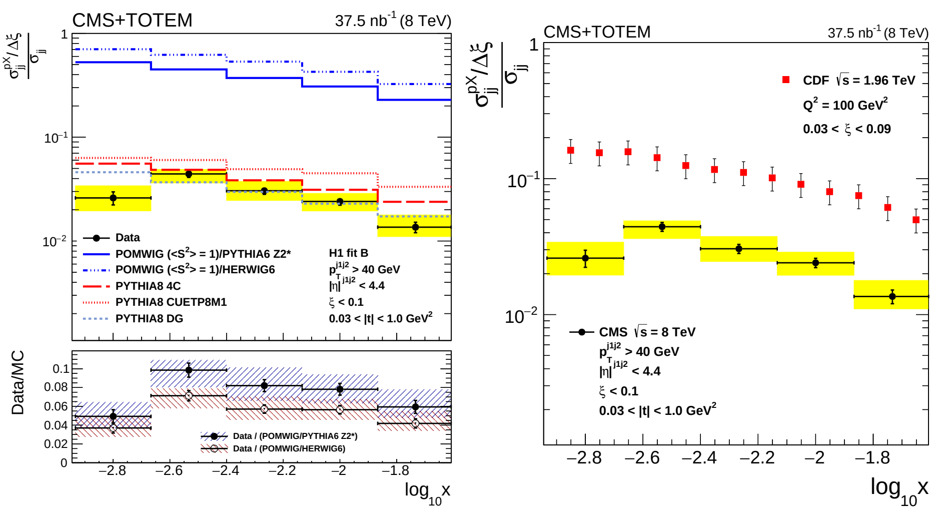

Fig. 10. (Colour on-line) Ratio per unit of ξ of the SD and inclusive dijet cross sections in the region $\xi < 0.1$ and $0.03 < |t| < 1$ GeV^2, compared to the predictions from the different models for the ratio between the SD and ND cross sections. Left: Pomwig is shown with no correction for the RG survival probability ($\langle S^2 \rangle = 1$). Right: Ratio per unit of x of the SD and inclusive dijet cross sections. The red points represent the results at 1.96 TeV [29]. Taken from Ref. [23].

5. Conclusion

The ATLAS and CMS experiments at the LHC allow for extensive tests of soft QCD. The predictions from MC event generators still show visible discrepancies when compared to the soft QCD resent results.

REFERENCES

[1] ATLAS Collaboration, *JINST* **3**, S08003 (2008).

[2] CMS Collaboration, *JINST* **3**, S08004 (2008).

[3] L. Evans, P. Bryant, *JINST* **3**, S08001 (2008).

[4] ATLAS Collaboration, *Phys. Lett. B* **790**, 595 (2019).

[5] CMS Collaboration, *Eur. Phys. J. C* **80**, 41 (2020).

[6] T. Sjöstrand *et al.*, *Comput. Phys. Commun.* **178**, 852 (2008).

[7] ATLAS Collaboration, *Eur. Phys. J. C* **79**, 666 (2019).

[8] S. Alioli *et al.*, *J. High Energy Phys.* **1006**, 043 (2010).

[9] T. Gleisberg *et al.*, *J. High Energy Phys.* **0902**, 007 (2009).

[10] M. Bahr *et al.*, *Eur. Phys. J. C* **58**, 639 (2008).

[11] ATLAS Collaboration, *Eur. Phys. J. C* **74**, 3195 (2014).

[12] CDF Collaboration, *Phys. Rev. D* **82**, 034001 (2010).

[13] CMS Collaboration, *Eur. Phys. J. C* **72**, 2080 (2012).

[14] CMS Collaboration, *J. High Energy Phys.* **1807**, 032 (2018).

[15] CMS Collaboration, *Eur. Phys. J. C* **76**, 155 (2016).

[16] M.H. Seymour, A. Siodmok, *J. High Energy Phys.* **1310**, 113 (2013).

[17] CMS Collaboration, *Eur. Phys. J. C* **79**, 123 (2019).

[18] CMS Collaboration, *Eur. Phys. J. C* **79**, 893 (2019).

[19] ATLAS Collaboration, *J. High Energy Phys.* **2002**, 042 (2020).

[20] ATLAS Collaboration, ATL-PHYS-PUB-2012-003, CERN, 2012.

[21] ATLAS Collaboration, ATL-PHYS-PUB-2016-017, CERN, 2016.

[22] CMS Collaboration, *Phys. Rev. D* **92**, 012003 (2015).

[23] CMS and Totem collaborations, `arXiv:2002.12146 [hep-ex]`, submitted to *Eur. Phys. J. C.*

[24] B.E. Cox, J.R. Forshaw, *Comput. Phys. Commun.* **144**, 104 (2002).

[25] CMS Collaboration, *Eur. Phys. J. C* **76**, 155 (2016).

[26] C.O. Rasmussen, T. Sjöstrand, *J. High Energy Phys.* **1602**, 142 (2016).

[27] T. Sjöstrand *et al.*, *J. High Energy Phys.* **0605**, 026 (2006).

[28] G. Corcella *et al.*, *J. High Energy Phys.* **0101**, 010 (2001).

[29] CDF Collaboration, *Phys. Rev. D* **86**, 032009 (2012).